Photocharging and Band Gap Narrowing Effects on the Performance of Plasmonic Photoelectrodes in Dye-Sensitized Solar Cells

Julio Villanueva-Cab,*[,†] Paul Olalde-Velasco,*[,†] Alfredo Romero-Contreras,[†] Zengqing Zhuo,[‡,§] Feng Pan,[§] Sandra E. Rodil,[∥] Wanli Yang,[‡] and Umapada Pal[†]

[†]Instituto de Física, Benemérita Universidad Autónoma de Puebla, Apdo. Postal J-48, Puebla, Puebla 72570, Mexico
[‡]Advanced Light Source, Lawrence Berkeley National Laboratory, 1 Cyclotron Road, Berkeley, California 94720, United States
[§]School of Advanced Materials, Peking University, Shenzhen Graduate School, Shenzhen 518055, People's Republic of China
[∥]Instituto de Investigaciones en Materiales, Universidad Nacional Autónoma de México, Mexico City 04510, Mexico

S *Supporting Information*

ABSTRACT: The incorporation of plasmonic nanostructures in active electrodes has become one of the most attractive ways to enhance the photoconversion efficiency (PCE) of dye-sensitized solar cells (DSSCs). Although an enhancement of PCE because of the incorporation of plasmonic nanostructures of different sizes, either bare or coated, has been demonstrated, the fundamental mechanisms associated to such enhancement are still unclear. Besides, the photocurrent enhancement of plasmonic DSSCs is frequently associated to the strong surface plasmon resonance (SPR) absorption of metal nanoparticles. In this work, through oxygen K-edge soft X-ray absorption and emission spectroscopies of plasmonic electrodes and electrodynamical characterization of the fabricated cells, we demonstrate a band gap narrowing and photocharging effect on the plasmonic electrodes that definitely contribute to the PCE enhancement in plasmonic DSSCs. The incorporation of bare metal nanoparticles in active metal−oxide semiconductor electrodes such as TiO$_2$ in optimum concentration causes an upward shift of its valence band edge, reducing its effective band gap energy and enhancing the short-circuit current of DSSCs. On the other hand, small perturbation-based stepped light-induced transient measurements of photovoltage and photocurrent of the operating DSSCs revealed an upward shift of quasi-Fermi level of photoelectrodes because of the photocharging effect induced by the incorporated metal nanoparticles. The upward shift of the quasi-Fermi level causes an increase in open-circuit voltage (V_{OC}), nullifying the effect of band gap reduction. The short-circuit photocurrent enhancement was controlled by the band gap narrowing, screening the SPR contribution. The results presented in this work not only clarify the contribution of SPR absorption in plasmonic DSSCs, but also highlight the importance of considering the corrections in the effective base voltage because of the quasi-Fermi level band shift during the estimation of the transport and recombination parameters of an assembled DSSC.

KEYWORDS: *light conversion, gold-incorporated electrodes, photocharging, band gap narrowing, synchrotron-based X-ray spectroscopies, electrodynamical characterization*
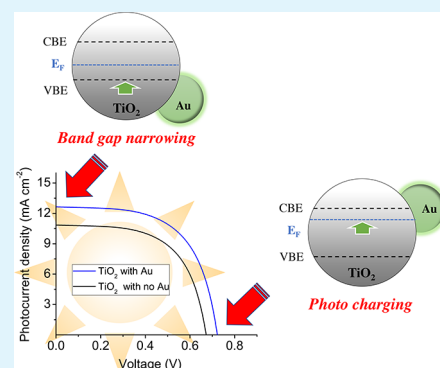
1. INTRODUCTION

Dye-sensitized solar cells (DSSCs)[1] present an attractive alternative to traditional inorganic thin-film-based photovoltaic devices because of their simpler manufacturing process and utilization of low purity components. The performance of DSSCs is established by the combination of good visible-light harvesting, efficient charge separation, faster charge transport, and slow recombination. Such a combination is achieved in an electrochemical system by introducing a high ion-conducting electrolyte into the electron-conducting material which serves as the electrode. In DSSCs, the electron-conducting material is conventionally a mesoporous oxide semiconductor such as TiO$_2$ or ZnO, whereas the ion-conducting electrolyte is generally an iodide/triiodide redox couple.[2] Efficient light harvesting in the visible range is achieved by adsorbing a suitable dye at the semiconductor surface. In DSSCs, light absorption (by the dye molecules) and electron transport (in the semiconductor oxide) processes do not take place in the same material, contrary to the single crystal solar cells. This offers the advantage of using different semiconductor nanostructures (like nanoparticles, core−shell, and one-/three-dimensional nanostructures) to increase the effective surface area of the electrodes for dye adsorption, reduce charge recombination, and improve charge transport.[3,4] Moreover, it allows the incorporation of new materials in the electrodes to improve their light absorption efficiencies. For example,

different dyes[5−7] and quantum dots[8,9] have been tested to improve the photocollection efficiency of DSSCs. One of the most substantial improvements made in thin-film solar cells in recent times is through the incorporation of plasmonic nanostructures (typically silver or gold nanoparticles), which enhances the photoabsorption capacity and reduces the physical thickness of the absorber layers.[10] For DSSCs, the incorporation of such plasmonic nanostructures enhances the light absorption cross section of the dye molecules and induces the photocharging effect.[11] The plasmonic nanostructures of different geometries/morphologies have been tested for the enhancement of DSSC efficiency, exploiting the localized surface plasmon resonance (SPR) characteristic of the noble metal nanostructures.[12−19] However, there exists no report in the literature on how the incorporation of metal nanostructures affects the electronic structure of the DSSC photoelectrodes. Moreover, the contribution of the photocharging effect, especially in the analysis of the transport and recombination parameters of DSSCs because of the incorporation of uncapped metallic nanostructures has not been appropriately studied. Although metals such as Pt in DSSC counter electrodes quickly discharge electrons to the surrounding medium, the incorporated metal nanoparticles (e.g., Ag and Au) in active electrodes store a fraction of the electrons captured from the photoexcited semiconductor nanoparticles.[20,21] The stored electrons, whose density depends on the size of metal nanoparticles, experience charge equilibration with the photoexcited semiconductor and shift their quasi-Fermi level to more negative potentials. For example, Fermi level shifts (and hence their corresponding photovoltages) around 20 and 60 meV have been observed when TiO_2 films were coupled with bare gold nanoparticles of 8 and 3 nm, respectively.[21] To distinguish the plasmonic contribution from the photocharging effect, Choi et al.[11] covered Au nanoparticles (∼5 nm) with thin (∼1 nm thick) layers of SiO_2 and TiO_2 and tracked their influence on DSSCs. They concluded: (i) the SiO_2 isolating layer acts as a barrier, which prevents electron charging of the metal core, consequently exhibiting only surface plasmon effects and (ii) a TiO_2 semiconducting layer allows electron transfer to the Au core, providing electron charging of the core. Additionally, it is also believed that the capping layer prevents the problems associated with the recombination and back reaction of the photogenerated carriers in DSSCs.[15,22−27] The highest efficiency improvements were achieved with 5−50 nm Au nanoparticles, although the contributions of the plasmonic, photocharging, and light scattering effects were seen to be different for the nanoparticles of different sizes.[27] However, to the best of our knowledge, there exist no information in the literature on how the incorporation of bare noble metal nanoparticles in the semiconducting active electrode of a DSSC alters its electronic states, affecting its light absorption capacity and hence the performance of the DSSC.

Synchrotron-based X-ray spectroscopies are invaluable element-specific tools to investigate the electronic structure of materials. Among them, soft X-ray absorption spectroscopy (XAS) and normal X-ray emission spectroscopy (NXES) are becoming increasingly important in researches related to energy materials. The inherent chemical and orbital selectivity [granted through the electric dipolar selection rules $(\Delta l = 1)$] of core-level X-ray spectroscopy allows a direct probe of element-specific unoccupied and occupied electronic states.[28,29] For example, the XAS and NXES spectra at the oxygen K-edge reflect (through the 1s−2p electronic transitions) the conduction and valence bands with the oxygen 2p character, respectively. In other words, they mirror the partial density of states of oxygen 2p of a material.[29,30]

In a previous publication,[31] we demonstrated a deterioration of the photovoltaic performance of DSSCs on the incorporation of bare Au nanoparticles at the top of the TiO_2 electrodes. The photovoltaic performance of DSSCs deteriorates with the increase in Au content. On the other hand, the common perception that bare Au nanoparticles act as recombination or back reaction centers does not fully explain the observed photovoltaic behaviors of the plasmonic DSSCs. In the present study, monodispersed bare Au nanoparticles of ∼27 nm average size were incorporated into mesoporous TiO_2 photoanodes in different concentrations to elucidate which of the earlier mentioned effects (plasmonic, photocharging, carrier recombination) have significant contribution in the performance of DSSCs upon the incorporation of plasmonic nanoparticles. The introduction of an optimum concentration of Au nanoparticles in the photoanode is seen to improve the short-circuit photocurrent, open-circuit voltage, and fill factor, leading to an overall increase in the photovoltaic performance of the fabricated DSSCs. The stepped light-induced transient measurements (SLITM) of photovoltage and photocurrent were utilized to determine the contribution of Au nanoparticle incorporation (in the photoelectrodes) to the electron lifetime and photocharging (Fermi-level shift) of the assembled devices. Photoelectrodes of ∼2.5 μm thickness were utilized for fabricating devices to minimize the loss of photoinjected charge carriers because of their recombination at the Au−electrolyte interface. Synchrotron-based oxygen K-edge XAS and NXES were utilized to investigate the relative energy positions of the conduction and valence bands of TiO_2 photoanodes fabricated with and without Au nanoparticles, respectively. The obtained results indicate that the enhanced performance of the DSSCs fabricated by incorporating bare Au nanoparticles in optimum concentration is due to an increase in both the short-circuit photocurrent and the open-circuit voltage. The increase in the short-circuit photocurrent is attributed to the reduction in the effective band gap of the TiO_2 electrodes, as observed by the external quantum efficiency (EQE) measurements and oxygen K-edge X-ray experiments. On the other hand, the increase of open-circuit voltage is associated to a shift of the quasi-Fermi level of TiO_2 photoelectrodes because of the incorporation of Au nanoparticles (photocharging effect).

2. EXPERIMENTAL SECTION

2.1. Materials and Methods. Gold(III) chloride (HAuCl$_4$·H$_2$O, 99.999%), sodium borohydride (NaBH$_4$, 99.99%), L-ascorbic acid (AA, ≥ 99%), cetyltrimethylammonium chloride solution (CTAC, 25 wt % in H$_2$O), methyl ether thiol (mPEG-t, av M_w = 6000), and absolute ethanol (>99%) used for the synthesis of gold nanoparticles were purchased from Sigma-Aldrich, Mexico. TiO$_2$ paste (18NR-T) and Z907 dye were purchased from Dyesol.

2.2. Synthesis of Au Nanoparticles. Spherical Au nanoparticles of ∼27 nm average size were synthesized by seed-mediated growth, following the procedure reported in our previous work.[32] In brief, first, Au clusters were prepared by adding 50 μL of Au-ion solution (100 mM) in 5 mL of aqueous CTAC solution (100 mM), followed by the addition of 200 μL of NaBH$_4$ solution (20 mM) under magnetic agitation (for 5 min). This cluster solution was utilized to fabricate Au seeds of about 10 nm size. For this, first, 2.25 mL of the AA solution (100 mM) was added into a 500 mL CTAC solution

(100 mM) and homogenized under magnetic agitation for 5 min. Then, 5 mL of the previously prepared cluster solution was added to it. Under vigorous magnetic agitation, a 12.5 mL of Au-ion solution (10 mM) was slowly added to the mixture. This seed solution containing Au nanoparticles of about 10 nm average size was used to fabricate bigger (~27 nm av size) Au particles. For this, about 3.25 mL of the AA solution (100 mM) was added to a 500 mL of CTAC solution (100 mM) under magnetic agitation. Then, 30 mL of the previously prepared Au seed solution was added to it. To this mixture, about 18.5 mL of Au-ion solution (10 mM) was added very slowly (~0.5 mL/min) under mild agitation. The addition of Au-ion solution was stopped when the reaction solution turned transparent and its color changed from dark gray to red. Keeping the resulting colloidal solution under agitation for a further 30 min, the formed Au particles were separated by centrifugation (10 000 rpm, 20 min) and redispersed in a fresh CTAC solution of 10 mM.

For transferring the formed Au nanoparticles into ethanol, they were separated again by centrifugation and redispersed again in CTAC solution (10 mM) containing mPEG-t (20 mM). After 24 h, the nanoparticles were separated by centrifugation and redispersed in 15 mL of absolute ethanol. The final gold concentration in the ethanol solution was estimated to be about 2.46 mg/mL.

2.3. Device Fabrication. Diluted TiO_2 pastes were prepared by mixing 0.5 g of Dysol TiO_2 paste (18NR-T) and 2 mL of anhydrous ethanol (with and without Au nanoparticles). For the case of Au-incorporated TiO_2 pastes, x mL (with x = 0, 0.5, 1.0, and 2.0 mL) of the ethanolic Au colloidal solution, containing Au nanoparticles of ~27 nm average size [estimated through dynamic light scattering (DLS, Malvern), Figure 1a], was used. Then, the diluted pastes were
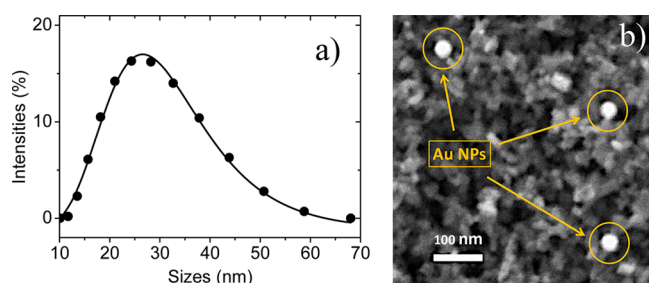

Figure 1. (a) DLS size distribution of fabricated colloidal Au nanoparticles showing a maximum around 26.56 nm, with the standard deviation of ±9.71 nm. (b) Typical SEM image of an Au nanoparticle-incorporated TiO_2 film (after sintering). The spherical brighter spots in the image (encircled) correspond to the Au nanoparticles.

reduced to one-third of their original volume under stirring at 70 °C over a hotplate. The TiO_2 films of about 0.25 cm² area with and without Au nanoparticles were fabricated by depositing the corresponding pastes onto transparent conducting oxide (TCO)-coated glass substrates (F-doped SnO_2; 10 Ω/sq) through screen printing. After air-drying, the deposited layers were sintered in air at

500 °C for 1 h. The average thickness of the fabricated nanocrystalline TiO_2 layers was about 2.5 μm (measured by a Dektak II profilometer). The presence of spherical-shaped Au nanoparticles in the TiO_2 films was confirmed by scanning electron microscopy (SEM, JEOL-JEM 211F, operating at 200 keV; Figure 1b). While cooling, the films were taken out of the annealing furnace at 80−100 °C and immersed in a solution of acetonitrile/*tert*-butyl alcohol (1:1, v/v) containing 0.3 mM Z907 dye for 16 h. A Shimadzu, UV-3101PC double-beam UV–vis–NIR spectrophotometer was used to record the absorption spectra of the TiO_2 films fabricated with and without Au nanoparticles before and after dye loading (Figure 2). The semitransparent counter electrodes were prepared by spreading two drops of 5 mM H_2PtCl_6 solution in 2-propanol over the TCO substrates and their subsequent firing at 450 °C for 1 h. The electrode (TiO_2 film with and without Au) and the Pt-covered counter electrode were then sandwiched together using a 25 μm thick thermoplastic (Surlyn, Dupont grade 1702). After introducing the electrolyte solution into the sandwiched electrodes, the predrilled holes of the counter electrode were sealed using small pieces of corning glass and thermoplastic. The electrolyte used in the DSSCs contained 0.6 M 1-butyl-3-methylimidazolium iodide and 0.03 M iodine in acetonitrile/valeronitrile (85:15, v/v %).

2.4. Device Characterization. The fabricated devices were characterized at room temperature using a setup consisting of a 450 W ozone-free Xe lamp (LOT-Oriel) with a water filter. The setup was calibrated to an irradiance of 100 mW cm⁻² at an equivalent air mass AM 1.5G on the surface of the solar cell; the intensity was calibrated using a certified 4 cm² monocrystalline silicon reference cell with an incorporated KG-5 filter. No mask was used during the photovoltaic characterization of the DSSCs. The quantum efficiency measurements were performed on the DSSCs with and without Au nanoparticles in a Newport quantum efficiency measurement system (QEPVSI-B) equipped with a bias light amplifier.

The SLITM of photovoltage and photocurrent were used to estimate the electron lifetime, transport time, and charge density of the fabricated DSSCs.[31,33] The DSSCs were probed with a stepped modulated laser or an LED beam of 630 nm wavelength (probe) superimposed on a relatively large background (bias) illumination, also with a 630 nm beam. The probe and the bias laser lights entered the cells through the electrode side (TCO substrate of TCO + TiO_2). The photovoltage decay because of the probe light was recorded (using a DPO70404 Tektronix oscilloscope) and used to fit a single exponential decay with an exponent $-t/\tau$, where τ is the fitting parameter, termed as electron lifetime. A similar procedure was followed to estimate the electron transport time. However, in this case, the measurements were performed under a short-circuit condition while recording the photocurrent transient.[31,33,34] To obtain the statistical variations of the obtained time constants (transport and recombination), each time constant was measured and fitted at least five times (using a DPO70404 Tektronix oscilloscope). The photovoltage/photocurrent measurements at the associated biases were also recorded. The steady-state photoinjected electron density in the TiO_2 films was estimated from the relation $n = T_\alpha J_{SC}\tau/(qd(1-P))$,[35] where T_α is the thermodynamic factor,[36,37] J_{SC} is the
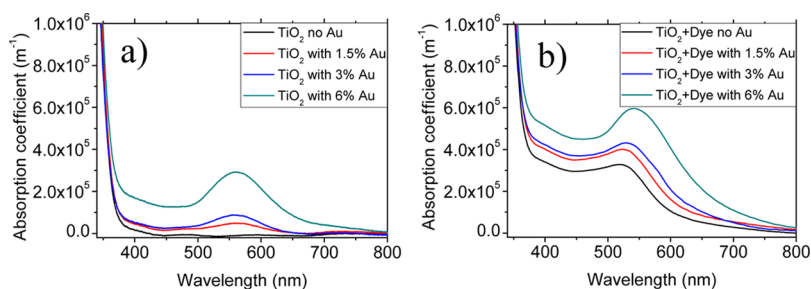

Figure 2. Absorption spectra of the TiO_2 films (all of ~2.5 μm thickness) with and without Au nanoparticles (~27 nm): (a) before and (b) after dye (Z907) loading.
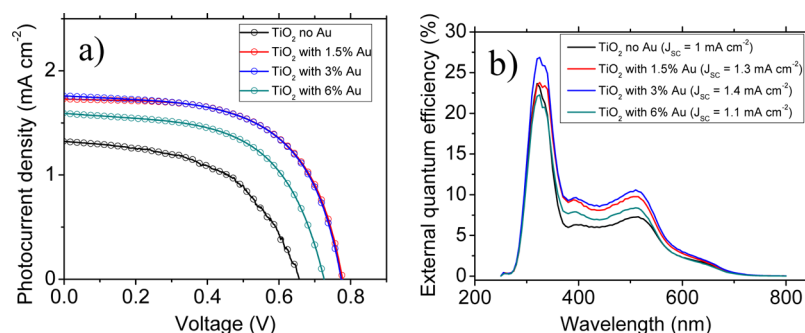
Figure 3. (a) Current density vs voltage plots for the representative devices showing an improvement in photovoltaic performance. (b) EQE for the representative devices showing an improvement in the photocurrent because of the incorporation of Au nanoparticles into the TiO$_2$ electrode. The J_{SC} values calculated at AM 1.5 solar irradiation are also included.

Table 1. Summary of Photovoltaic Parameters for the Devices Fabricated With and Without Au Nanoparticles[a]

Au wt %	J_{SC} (mA cm^{-2})	V_{OC} (V)	FF	P_{max} (mW cm^{-2})
0	1.380 ± 0.260	0.653 ± 0.047	0.556 ± 0.021	0.509 ± 0.107
1.5	1.544 ± 0.274	0.753 ± 0.023	0.591 ± 0.022	0.690 ± 0.152
3	1.835 ± 0.107	0.763 ± 0.015	0.599 ± 0.003	0.839 ± 0.036
6	1.355 ± 0.211	0.708 ± 0.028	0.581 ± 0.014	0.558 ± 0.096

[a]The values of each parameter were estimated from the average of at least four samples.

short-circuit photocurrent density established by the bias light, P is the film porosity ($P = 0.6$), q is the absolute value of the electron charge, τ is the electron transport time for electron density at short circuit or the lifetime for electron charge density at open-circuit conditions. The thermodynamic factor,[36,37] α, which is related to the steepness of the trap distribution or the average trap depth and related to temperature by $\alpha^{-1} = T_0/T$, where T_0 is the characteristic temperature, was assumed to be constant for all the samples. Neutral density filters were used to vary the intensity of illumination, to generate a plot of electron lifetime, transport time, and charge density as the function of photovoltage. The plots of charge density as the function of photovoltage were used to compare (after band shift corrections) the lifetimes and transport times of the TiO$_2$ electrodes (with and without Au) at the same quasi-Fermi level. The open-circuit voltage and short-circuit current were recorded for each illumination intensity.

2.5. XAS and NXES Measurements. XAS and NXES measurements were performed in the high-efficiency iRIXS endstation at beamline 8.0.1 of the Advanced Light Source at Lawrence Berkeley National Laboratory.[38] Its spherical grating monochromator delivers 10^{12} photons/second with linear polarization, with a resolving power up to 6000.[39] The oxygen K-edge XAS measurements were collected at room temperature in the total fluorescence yield (TFY) mode, with the probe depth of 100 nm. All spectra have been normalized to the photon flux recorded by a clean gold mesh in the upper stream of the experimental chamber. The oxygen K-edge NXES spectra were collected through the high-transmission X-ray spectrometer, with the excitation energy of 580 eV. The resolving power is better than 1500 for the XAS experiments.

3. RESULTS AND DISCUSSION

Figure 1 shows the DLS-estimated size distribution of the fabricated Au nanoparticles (Figure 1a) and a typical SEM image of the Au nanoparticles incorporated into the TiO$_2$ film (Figure 1b) after sintering in air at 500 °C for 1 h. As can be noticed in Figure 1, the average hydrodynamic diameter of the fabricated Au nanoparticles is around 27 nm, whereas their average size estimated from the SEM image is around 32 nm. As can be noticed from the SEM image (Figure 1b), there is no agglomeration of Au nanoparticles or change in their spherical

shape after the sintering of the electrodes prepared with different Au contents of Au nanoparticles (Figure S1).

To study the effect of the incorporation of metallic nanoparticles on the photovoltaic performance of DSSC electrodes, we used a DSSC with no Au nanoparticles as reference and DSSCs containing different amounts of Au nanoparticles (around 1.5, 3, and 6 wt % of TiO$_2$ powder). Figure 2 shows the absorption spectra of the representative TiO$_2$ electrodes (~2.5 μm thick) with and without Au nanoparticles before (Figure 2a) and after (Figure 2b) the dye (Z907) loading. As can be noticed, an absorption band peaked around 560 nm (for all the curves in Figure 2a) appears when Au is incorporated into the TiO$_2$ matrix. The band corresponds to the SPR of Au nanoparticles. After sensitization, the overall intensity of the absorption band for both types of films (with and without Au nanoparticles) increased noticeably. However, a gradual increase in absorption band intensity can be observed with the increase of Au content in the sensitized films containing Au nanoparticles, indicating an overall increase of light harvesting, which, in assembled devices, could be transformed to a higher photovoltaic performance (efficiency). The absorption maximum of the TiO$_2$ films containing Au nanoparticles after their sensitization remain in between the absorption maximum of the Z907 dye (around 520 nm) and the SPR position (~560 nm) of Au nanoparticles, gradually shifting toward the latter with the increase of the Au nanoparticle content.

As mentioned before, thin photoelectrodes (~2.5 μm) were utilized for fabricating the devices to minimize the loss of photoinjected charges because of their recombination at the Au−electrolyte interface (see Figure S2, Supporting Information). As can be seen in Figure S2 (Supporting Information), under continuous illumination, the V_{OC} of the devices fabricated with thicker electrodes [~12 μm, around the optimum thickness for the highest photoconversion efficiency (PCE)] containing Au nanoparticles takes more than 60 min to get stabilized (steady state). This makes the small perturbation technique almost impossible to apply, as it can

be applied only when the V_{OC} under fixed illumination reaches a steady state. Although the effect also occurs for the devices fabricated with thinner electrodes (containing Au nanoparticles), the V_{OC} under illumination stabilizes rather quickly. In DSSCs with thin plasmonic photoelectrodes (~2.5 μm), the V_{OC} reaches its steady state within about 4 min of illumination (Figure S2, in the Supporting Information).

Figure 3 shows the current density (J_{SC}) versus voltage and EQE plots for the representative devices fabricated with and without Au nanoparticles in the TiO_2 electrodes. As can be noticed in the current density versus voltage curves, shown in Figure 3a, the photovoltaic performance of the cells fabricated with TiO_2 electrodes increased noticeably with the incorporation of Au nanoparticles. The efficiency of the plasmonic DSSCs is maximum when the photoelectrodes contain Au nanoparticles in the 1.5–3.0 wt % (within experimental errors) range. In Table 1, we compare the averaged photovoltaic parameters of a set of four similar samples corresponding to each system, that is, cells without and with Au nanoparticles. In general, increases in the short-circuit photocurrent (J_{SC}), open-circuit voltage (V_{OC}), and fill factor (FF) on Au incorporation were observed for most of the Au-incorporated DSSCs, reaching an overall conversion efficiency maximum for the sample containing 3% of Au. To be more specific, J_{SC} and V_{OC} increased by around 33% (0.455 mA cm^{-2}) and 17% (110 mV), respectively, and the FF increased by around 7%. The overall increase in the maximum power conversion (P_{max}) for this particular Au content was around 64%. As can be noticed from Figure 3b, the increase in the EQE response (with respect to the reference) of the cells is not linear with the increase of Au content in the photoelectrode. Figure 3b also shows the J_{SC} values obtained from the integration of EQE over the AM 1.5 G solar irradiation spectra. Although all the values of J_{SC} calculated from the EQE spectra do not match with the ones obtained from the $J–V$ curves, they follow the same trend (Table 1 and Figure 3b). Another important thing to be noticed in Figure 3b is the variation of band gap energy of TiO_2 because of the Au nanoparticle incorporation. As has been elaborated by Helmers et al.,[40] the band gap of the TiO_2 film electrodes must remain in between the wavelengths of 330 and 350 nm. On Au nanoparticle incorporation, although a decrease in the band gap of TiO_2 (with respect to the reference) is expected, the observed decrease (higher wavelength shift of absorption edge, Figure 3b) is not linear with the increase of Au content in the photoelectrodes. In fact, the highest decrease of band gap is observed for the TiO_2 electrode containing 3 wt % Au. Apparently, the light absorption capacity of the photoelectrodes (on the overall range) increases until 3 wt % of Au and thereafter decreases returning to its original value (Figure 3b). Although a variation in band gap energy can occur because of the shift of the conduction/valence band of a semiconductor in direct contact with a metal, as observed for ZnO with incorporated Au nanoparticles,[41] the phenomenon and its effect on the photovoltaic parameters for DSCCs have not been studied. Although the increase in J_{SC} in plasmonic DSSCs is frequently associated to the SPR of Au nanoparticles, which is believed to increase the light-harvesting efficiency of the sensitized electrodes,[12–19] an increase in the absorption of visible light because of the reduction of the band gap in TiO_2 electrodes upon the incorporation of Au nanoparticles has not been considered before. To determine the extent of band gap reduction in TiO_2 electrodes because of the Au nanoparticle

incorporation, we utilized a combination of NXES and XAS at the oxygen K-edge, as discussed in the later sections.

On the other hand, the increase in V_{OC} could be adjudicated to the photocharging effect of the metallic nanoparticles. This effect is normally observed on small metallic particles (3–8 nm) that shift the quasi-Fermi level of TiO_2 to more negative potentials.[11,21] However, highest efficiency improvements in plasmonic DSSCs have been achieved using Au nanoparticles of 5–50 nm sizes and ascribed to different mechanisms.[27] Therefore, understanding these involved mechanisms is of great scientific interest. In fact, the mechanism involved in the increase of V_{OC} in plasmonic DSSCs has not been studied in detail for uncapped metallic nanoparticles as large as ~27 nm. To give it a try, Choi et al.[11] utilized small Au nanoparticles (around 5 nm) capped with thin isolating (SiO_2) and semiconducting (TiO_2) layers (~1 nm thick) to separate the SPR and photocharging effects of Au nanoparticles in DSSCs. As has been mentioned in the Introduction section, it is believed that capping metallic nanoparticles with an insulating or semiconducting layer prevents the photogenerated electrons to recombine across the metal–electrolyte and metal–dye interfaces.[15,22–27] To elucidate whether bare Au nanoparticles of around 27 nm diameter contribute positively to the V_{OC} by the photocharging effect and limit the photovoltaic performance of DSSCs by increasing the recombination rate, we performed electrodynamic characterizations on DSSCs fabricated with and without Au nanoparticles. The open-circuit voltage versus electron charge density plots are normally used to determine any movements of the quasi-Fermi level [or conduction band edge (CBE)] of the TiO_2 electrode in DSSCs.[42] This is accomplished by knowing that the photogenerated charge density is solely determined by the difference between the CBE and the electron quasi-Fermi level under illumination. For example, at a fixed charge density, a higher V_{OC} indicates an upward shift of the quasi-Fermi level. Likewise, at a fixed charge density, a lower V_{OC} indicates a downward shift of the quasi-Fermi level.[42] As the quasi-Fermi level of the redox couple is traditionally assumed to be unchanged, at a fixed charge density, any movement of the quasi-Fermi level of the TiO_2 electrode can also be interpreted as a movement (in the same direction) of the CBE.

Figure 4 shows the open-circuit voltage versus electron charge density plots for representative cells fabricated with and without Au nanoparticles, where the cell with no Au is
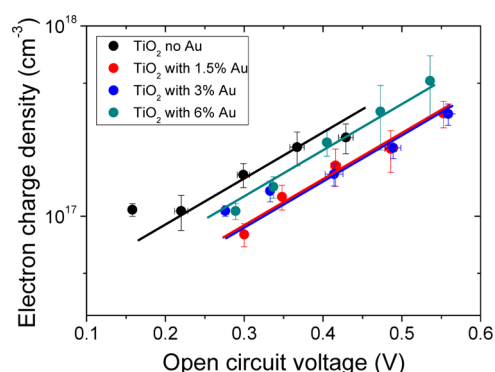

Figure 4. Open-circuit voltage vs electron charge density plots for representative cells fabricated with and without Au nanoparticles. The lines correspond to the best fit of the experimental data to a semilogarithmic function log(electron charge density)–V_{OC}.

considered as the reference. As can be observed, the incorporation of Au nanoparticles in the TiO_2 matrix leads to an upward shift of the TiO_2 quasi-Fermi level, in agreement with previously reported observations made for larger Au nanoparticles (in the DSSC electrodes).[43] The upward shifts of the quasi-Fermi level were estimated to be around 108 meV for the electrodes containing 1.5 and 3.0 wt % of Au and about 42 meV for the electrodes containing 6.0 wt % of Au. Although these shifts did not reveal any linear correlation with the Au content in the electrodes, the V_{OC} of the fabricated devices increased in a similar fashion. The V_{OC} of the cells increased by 100, 110, and 55 mV with respect to the reference cell for the electrodes containing 1.5, 3.0, and 6.0 wt % of Au, respectively (see Table 1 and Figure 4). The observed difference between the increase in V_{OC} and the upward shift of the quasi-Fermi level might be due to the fluctuation in the measured V_{OC} values or due to an increase in the electron lifetime. As has been mentioned earlier, an upward shift of the TiO_2 quasi-Fermi level is normally adjudicated to a charging effect because of the Au nanoparticle incorporation.

Although the observed increases of J_{SC} and V_{OC} in DSSCs fabricated with Au nanoparticles could be generally explained through the effective reduction of band gap energy and upward shift of quasi-Fermi level in TiO_2 electrodes, a direct evidence of the band gap reduction is needed. Despite the currently ongoing debate on the direct or indirect nature of the band gap of TiO_2 in the anatase phase, the electronic band structure of TiO_2 is well understood in the sense that its band gap is between the occupied oxygen 2p and the unoccupied titanium 3d states.[44] However, because of the strong oxygen (ligand) 2p–titanium 3d hybridization, it is possible to energetically align the occupied and unoccupied oxygen 2p (ligand) states with the corresponding titanium 3d states as observed, respectively, by oxygen (ligand) K-edge and titanium ($L_{2,3}$ edges) NXES (occupied states)[28] and XAS (unoccupied states).[45] Therefore, the combination of the oxygen K-edge NXES and XAS spectra allows a direct estimation of the band gap from the oxygen 2p perspective. In fact, the estimation of the band gap of TiO_2 (and other oxides) by the combination of oxygen K-edge XAS and NXES is nowadays well-established.[30,46]

In Figure 5, we present the oxygen K-edge NXES (left) and XAS (right) spectra for the TiO_2 reference and the Au-containing films plotted on a common energy scale. For clarity, we only present an expanded view around the leading edges of both the oxygen K-edge NXES (left) and XAS (right) spectra, with the full-range spectra plotted in Figure S3 (Supporting Information). The XAS spectra were acquired in the TFY mode with a probe depth of about 100 nm. We observed that the unoccupied oxygen 2p states barely move in energy upon Au inclusion. This can be verified by noticing that the leading edges of the XAS spectra almost fully overlapped (although there are subtle variations; see Figure S5 in the Supporting Information). On the other hand, the occupied oxygen 2p states (NXES spectra in Figure 5) clearly shift to higher photon energies upon Au incorporation into the nano-structured TiO_2 matrix (see Figure S4 in the Supporting Information). We can see that the maximum shift to higher energies in the oxygen K-edge NXES spectra (~200 meV) is reached for the film containing 1.5 wt % Au. The energy shift for the film containing 3 wt % Au is essentially the same as that for the 1.5 wt % Au-containing sample. However, interestingly, it is reduced for the sample containing 6 wt % Au (ca. 100
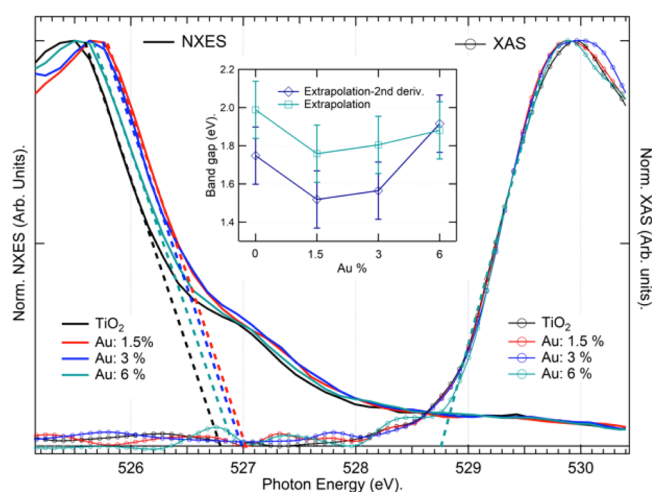

Figure 5. Upper panel: Band gap evolution of the TiO_2 thin films as a function of Au nanoparticle content as determined from the combination of oxygen K-edge XAS (left) and NXES (right) spectra. The band gap is estimated from the difference in energy between the intersections of the dashed lines in the energy axis. The dashed lines were obtained by extrapolating the edges' slopes in the NXES (left) and XAS (right) spectra. The inset in the figure contains the estimated band gaps.

meV). This behavior can be followed by looking at the variations of the edge in the NXES spectra and the position of maximum intensity in the spectra. On the other hand, although the absorption edges barely move in XAS, the variation in the maximum intensity position in the spectra is not systematic and subtle, as can be seen at the top of the XAS spectra.

Naturally, the abovementioned behavior in the energy shifts of the oxygen K-edge NXES and XAS spectra is reflected in the band gaps of the Au-containing films. The estimation of band gap energy by the combined NXES and XAS at the oxygen K-edges can be performed by several methods, which yield comparable results. In the most widely used method, the band gap is estimated from the difference in energies between the crossing points at the energy axis of the extrapolated slopes of the XAS and NXES spectra, as indicated in the dashed line in Figure 5. An alternative method involves the measurement of the difference in energy between the onsets of the XAS and NXES spectra, as identified by the second derivative of the spectra. To quantify the band gap evolution as a function of Au content in the nanostructured TiO_2 films, we estimated their band gaps by the extrapolation method and by another "hybrid method" that combines the extrapolation and the second derivative methods (see the Supporting Information for details). Results from such estimations are summarized in the inset of Figure 5. We observe, regardless of the method employed, that upon Au nanoparticle incorporation the band gap closes. In addition, we notice that the band gap values determined by the extrapolation method are about 0.25 eV larger than those determined by the second derivative method, except for the 6 wt % Au-containing film, for which the band gap as estimated by both methods is essentially the same. The systematic 0.25 eV difference and the similar result in the band gap for the 6 wt % Au sample are a consequence of the procedure employed by each method (see the Supporting Information). We employed both methods aiming to set upper and lower boundaries to the band gap values of our samples as obtained from oxygen K-edge soft X-ray spectroscopies. As the

band gap values obtained by both methods essentially follow the same trend, we will base our discussion around the extrapolation method values. For the reference sample (without Au nanoparticles), we found a band gap of 1.99 eV, which is in good agreement with a previously reported value of 2.1 eV obtained by the same method.[30] When Au nanoparticles are incorporated, we observe that for the film containing 1.5 wt % Au, the band gap value decreases to a value of 1.76 eV, which then increases for the films with 3 and 6 wt % with the values of 1.80 and 1.88 eV, respectively, as observed in the inset of Figure 5.

Table 2 summarizes the most important findings of this work. Interestingly, all the photovoltaic parameters related with

Table 2. Summary of Short-Circuit Photocurrent Density Increase ΔJ_{SC}, Open-Circuit Voltage Increase ΔV_{OC}, Quasi-Fermi Level Upward Shift ΔE_F, and Band Gap Reduction ΔE_g because of the Incorporation of Au Nanoparticles in TiO$_2$ Electrodes

Au wt %	ΔJ_{SC} (mA cm^{-2})	ΔV_{OC} (V)	ΔE_F (V)	ΔE_g (eV)
0	0	0	0	0
1.5	0.164	0.100	0.108	0.23
3	0.455	0.110	0.108	0.19
6	−0.025	0.055	0.042	0.11

the PCE (J_{SC} and V_{OC}) seem to follow the same trend as of the band gap evolution observed by oxygen K-edge NXES and XAS. As discussed earlier, a decrease of the band gap of TiO$_2$ leads to an overall increase in the light absorption of TiO$_2$ films, which could explain the observed increase (in most cases) in J_{SC} of the DSSCs upon the incorporation of Au nanoparticles in their active electrodes, as compared to the reference DSSCs fabricated without Au nanoparticle incorporation. However, we cannot discard the contributions of other factors to J_{SC} (Table 2), such as change in the light absorption

capacity because of the SRP of Au, variations in the charge injection efficiency because of the energetic alignments between the dye molecules and the CBE of TiO$_2$,[47] and changes in the charge collection efficiencies because of the variation in the carrier diffusion lengths. For example, the CBE of the TiO$_2$ electrode is normally placed around 1.0 eV from the electrolyte's quasi-Fermi redox level, indicating a maximum expected value of V_{OC} of around 1.0 V. Listorti et al.[47] reported that for the Z907 dye (the one used in this study), when the CBE is around 1.0 V (from the electrolyte), the electron injection efficiency is around 90% and, if this CBE is displaced by 100 mV toward the negative potential (displacing the CBE to 1.1 V from the electrolyte), a decrease in the injection efficiency from 90 to 70% is expected. On the other hand, from the electron lifetime and transport time values, we can obtain information on the change in the charge collection efficiencies. It is also important to mention that, in the cases of shifts in the quasi-Fermi level of the TiO$_2$ electrode because of any treatment or metal nanoparticle incorporation, such as in this work, it is necessary to make corrections in the time constant versus V_{OC} plots to compare the transport and recombination parameters at the same quasi-Fermi level.[42] In Figure 6, we show the variations of transport and recombination (life) times with the Au nanoparticle content before and after band shift corrections. As can be observed in Figure 6a, without band shift correction, for a fixed V_{OC}, the lifetime apparently increases up to 2 times (slow recombination) because of the Au nanoparticle incorporation, as has been reported previously,[43] leading to the wrong conclusion that an increase in lifetime also contributes to the enhancement of V_{OC}. Likewise, in Figure 6b, for the same V_{OC}, the transport time marginally increases up to 1.2-fold (slower transport) because of the Au nanoparticle incorporation. In fact, for the sample with the highest time constant variation (1.5 wt % of Au) at a particular V_{OC} (0.350 V), we expected a slight increase in the
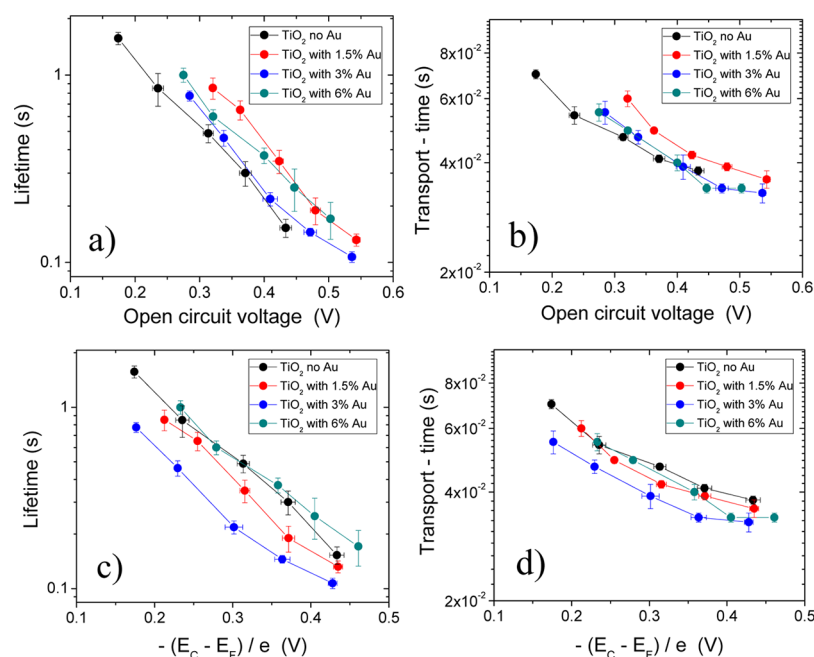

Figure 6. Semilogarithmic plots of life and transport times as obtained from the SLITM of photovoltage and photocurrent for DSSCs with different Au contents: (a) lifetime and (b) transport time vs open-circuit voltage; (c) lifetime and (d) transport time after band shift correction ($V_{OC} - \Delta E_F$).

electron collection efficiency, which can be roughly estimated through the relation $\eta_{cc} = 1 -$ transport time/lifetime,[48] leading to a wrong conclusion that the increase in the electron collection efficiency also contributes to the enhancement of J_{SC} in the DSSCs containing Au nanoparticles. On the contrary, when the band shift has been considered, at the same quasi-Fermi level, we observe a gradual decrease in the lifetime (faster recombination) for DSSCs with 1.5 and 3% of Au nanoparticle incorporation up to 2 times; after that, for the DSSCs with 6% of Au, the lifetime seems to match the values of the DSSCs with no Au nanoparticles. These observations lead to the conclusions that the decrease in the lifetime negatively contributes to the V_{OC}. Also, at the same quasi-Fermi level, the transport time marginally decreases up to 1.2 times (faster transport) with the Au nanoparticle incorporation. Again, as a comparison, for the sample with the highest variations in time constants (this time, 3 wt % of Au), at a fixed quasi-Fermi level (0.350 V), we expect a decrease in the electron collection efficiency, contributing negatively to the J_{SC}. As can be observed, contradictory conclusions can be reached whether or not band shifts are accounted for. In this context, it is important to highlight that even with the decrease in the electron injection efficiency and the decrease in the lifetime, maximum increases of about 33% in J_{SC} and of about 17% in V_{OC} were observed for the sample with 3% of Au, leading to the conclusion that the most important contributions to the J_{SC} and V_{OC} increases are respectively related to the band gap decrease and to the charging effect (upward shift of the TiO$_2$ quasi-Fermi level) of the TiO$_2$ + Au electrodes.

Figure 7 schematically summarizes the most important findings of the present study. An upward shift of the quasi-
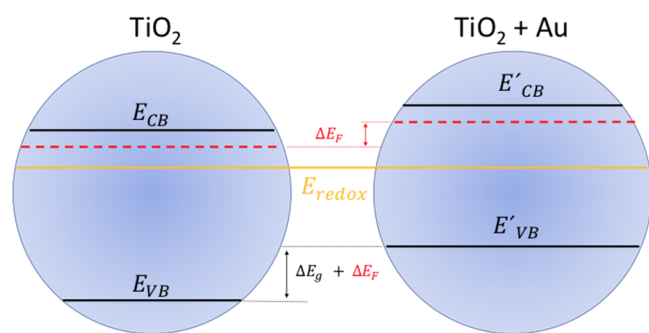

Figure 7. Proposed schematic representation of energy band diagrams of TiO$_2$ films with and without Au nanoparticles used as photoanodes for the fabrication of DSSCs. The band gap reduction ΔE_g increases the light absorption, whereas the upward shift ΔE_F contributes to an increase in the open-circuit voltage. Both effects contribute to an overall increase in the efficiency of DSSCs.

Fermi level leads to an increase of V_{OC} by about ΔE_F. At the same time, a decrease in the electron injection efficiency from the excited state of the dye (S$^+$) to the CBE of TiO$_2$ is expected (not shown in Figure 7). As can be observed from Table 2, the detected variations of J_{SC} with Au content correlate very well with the band gap energy ΔE_g variations. Therefore, assuming that no change in transport and recombination rates occurred because of the Au nanoparticle incorporation (see Figure 6), we can conclude that the change in the injection efficiency does not affect J_{SC} significantly. On the other hand, as has been detected by oxygen K-edge XAS and NXES, the band gap energy of unsensitized TiO$_2$ electrodes changes on incorporating bare Au nanoparticles.

Therefore, some changes can be expected on the performance of fabricated (real) devices, where the adsorbed dye molecules and the electrolyte solution are in contact with the gold nanoparticle-incorporated active electrode surface. For example, in a semiconductor in contact with an electrolyte, electric current initially flows across the junction until electronic equilibrium is reached, where the Fermi energy of the electrons in the solid semiconductor is equal to the redox potential of the liquid electrolyte.[49] Additionally, the dye adsorbed on the TiO$_2$ surface also modifies its quasi-Fermi level.[50] In such a case, a change in the quasi-Fermi level is also expected for the incorporated Au nanoparticle and the dye-loaded electrodes in contact with the electrolyte. For instance, an upward shift of the valence band edge of the TiO$_2$ electrode because of the Au nanoparticle incorporation must lead to an upward shift of the equilibrium Fermi level (or the quasi-Fermi level in dark), which reduces the separation between the CBE and the quasi-Fermi level in dark. The phenomenon in turn diminishes the maximum expected V_{OC} of the device. Therefore, to evaluate the contributions of plasmonic metal nanoparticles incorporated in the active electrode matrix of an assembled DSSC, it is essential to evaluate their contribution in the electronic structure of the semiconductor electrode, combined with the well-controlled deposition techniques for plasmonic metal[51,52] and TiO$_2$ nanostructures.[53] Although in the present study, we clearly demonstrate a change in the electronic band structure of TiO$_2$ from the oxygen 2p perspective because of the Au nanoparticle incorporation, further studies associated to the electronic band structure of titanium 3d, 4s states, and gold are required to have a more complete understanding of the phenomena occurring in plasmonic DSSCs.

4. CONCLUSIONS

In conclusion, through the oxygen K-edge X-ray absorption and emission spectroscopic studies, we demonstrate that Au nanoparticles incorporated in the active TiO$_2$ electrodes of plasmonic DSSCs interact with the occupied energy levels of TiO$_2$, leading to a decrease in the TiO$_2$ band gap through an upward shift of its valence band edge. Although for such a narrowing of band gap energy, a downshift of the quasi-Fermi level is expected, electrodynamical studies on the fabricated cells under operation (illumination) revealed rather an upward shift because of the photocharging effect in the metal nanoparticles, screening the effect of band gap narrowing. The upward shift of the quasi-Fermi level of TiO$_2$ contributes positively to the open-circuit voltage of the DSSCs, avoiding the reduction of the open-circuit voltage because of band gap narrowing. On the other hand, the short-circuit photocurrent follows an opposite trend to that of electrode band gap variation, indicating the band gap narrowing has a determinant (positive) effect on the short-circuit current values, whereas the contribution of the free electron plasmons of Au nanoparticles in the short-circuit current is marginal. The obtained results also highlight the importance of considering corrections in the effective base voltage because of the quasi-Fermi level band shift during the estimation of the transport and recombination parameters of an assembled DSSC.

■ ASSOCIATED CONTENT

Ⓢ Supporting Information

The Supporting Information is available free of charge on the ACS Publications website at DOI: 10.1021/acsami.8b10063.

SEM analysis of the composite electrodes, open-circuit voltage stability analysis, XAS and NXES measurement details, and estimation of the band gap by the "hybrid method" (PDF)

■ AUTHOR INFORMATION

Corresponding Authors
*E-mail: juliovc@ifuap.buap.mx (J.V.-C.).
*E-mail: paulolalde@gmail.com (P.O.-V.).

ORCID
Julio Villanueva-Cab: 0000-0002-6261-9197
Paul Olalde-Velasco: 0000-0003-0882-0778
Feng Pan: 0000-0002-8216-1339
Wanli Yang: 0000-0003-0666-8063
Umapada Pal: 0000-0002-5665-106X

Author Contributions
The manuscript was written through contributions of all authors. All authors have given approval to the final version of the manuscript.

Notes
The authors declare no competing financial interest.

■ REFERENCES

(1) O'Regan, B.; Grätzel, M. A Low-Cost, High-Efficiency Solar-Cell Based on Dye-Sensitized Colloidal TiO$_2$ Films. *Nature* **1991**, *353*, 737−740.

(2) Grätzel, M. The Advent of Mesoscopic Injection Solar Cells. *Prog. Photovoltaics* **2006**, *14*, 429−442.

(3) Zhang, Q.; Cao, G. Nanostructured Photoelectrodes for Dye-Sensitized Solar Cells. *Nano Today* **2011**, *6*, 91−109.

(4) Villanueva-Cab, J.; Jang, S.-R.; Halverson, A. F.; Zhu, K.; Frank, A. J. Trap-Free Transport in Ordered and Disordered TiO2 Nanostructures. *Nano Lett.* **2014**, *14*, 2305−2309.

(5) Wang, P.; Zakeeruddin, S. M.; Moser, J. E.; Nazeeruddin, M. K.; Sekiguchi, T.; Grätzel, M. A Stable Quasi-Solid-State Dye-Sensitized Solar Cell with an Amphiphilic Ruthenium Sensitizer and Polymer Gel Electrolyte. *Nat. Mater.* **2003**, *2*, 402−407.

(6) Nazeeruddin, M. K.; Bessho, T.; Cevey, L.; Ito, S.; Klein, C.; De Angelis, F.; Fantacci, S.; Comte, P.; Liska, P.; Imai, H.; Graetzel, M. A High Molar Extinction Coefficient Charge Transfer Sensitizer and its Application in Dye-Sensitized Solar Cell. *J. Photochem. Photobiol., A* **2007**, *185*, 331−337.

(7) Grätzel, M. Recent Advances in Sensitized Mesoscopic Solar Cells. *Acc. Chem. Res.* **2009**, *42*, 1788−1798.

(8) Mora-Seró, I.; Bisquert, J. Breakthroughs in the Development of Semiconductor-Sensitized Solar Cells. *J. Phys. Chem. Lett.* **2010**, *1*, 3046−3052.

(9) Sambur, J. B.; Novet, T.; Parkinson, B. A. Multiple Exciton Collection in a Sensitized Photovoltaic System. *Science* **2010**, *330*, 63−66.

(10) Atwater, H. A.; Polman, A. Plasmonics for improved photovoltaic devices. *Nat. Mater.* **2010**, *9*, 205−213.

(11) Choi, H.; Chen, W. T.; Kamat, P. V. Know Thy Nano Neighbor. Plasmonic versus Electron Charging Effects of Metal Nanoparticles in Dye-Sensitized Solar Cells. *ACS Nano* **2012**, *6*, 4418−4427.

(12) Zhao, G.; Kozuka, H.; Yoko, T. Effects of the incorporation of silver and gold nanoparticles on the photoanodic properties of rose bengal sensitized TiO2 film electrodes prepared by sol-gel method. *Sol. Energy Mater. Sol. Cells* **1997**, *46*, 219−231.

(13) Wen, C.; Ishikawa, K.; Kishima, M.; Yamada, K. Effects of silver particles on the photovoltaic properties of dye-sensitized TiO2 thin films. *Sol. Energy Mater. Sol. Cells* **2000**, *61*, 339−351.

(14) Hou, W.; Pavaskar, P.; Liu, Z.; Theiss, J.; Aykol, M.; Cronin, S. B. Plasmon Resonant Enhancement of Dye Sensitized Solar Cells. *Energy Environ. Sci.* **2011**, *4*, 4650−4655.

(15) Qi, J.; Dang, X.; Hammond, P. T.; Belcher, A. M. Highly Efficient Plasmon-Enhanced Dye-Sensitized Solar Cells through Metal@Oxide Core-Shell Nanostructure. *ACS Nano* **2011**, *5*, 7108−7116.

(16) Zarick, H. F.; Hurd, O.; Webb, J. A.; Hungerford, C.; Erwin, W. R.; Bardhan, R. Enhanced Efficiency in Dye-Sensitized Solar Cells with Shape-Controlled Plasmonic Nanostructures. *ACS Photonics* **2014**, *1*, 806−811.

(17) Yen, Y.-C.; Chen, P.-H.; Chen, J.-Z.; Chen, J.-A.; Lin, K.-J. Plasmon-Induced Efficiency Enhancement on Dye-Sensitized Solar Cell by a 3D TNW-AuNP Layer. *ACS Appl. Mater. Interfaces* **2015**, *7*, 1892−1898.

(18) Xu, Q.; Liu, F.; Liu, Y.; Cui, K.; Feng, X.; Zhang, W.; Huang, Y. Broadband Light Absorption Enhancement in Dye-Sensitized Solar Cells with Au-Ag Alloy Popcorn Nanoparticles. *Sci. Rep.* **2013**, *3*, 2112.

(19) Chang, S.; Li, Q.; Xiao, X.; Wong, K. Y.; Chen, T. Enhancement of Low Energy Sunlight Harvesting in Dye-Sensitized Solar Cells Using Plasmonic Gold Nanorods. *Energy Environ. Sci.* **2012**, *5*, 9444−9448.

(20) Oldfield, G.; Ung, T.; Mulvaney, P. Au@SnO2 Core-Shell Nanocapacitors. *Adv. Mater.* **2000**, *12*, 1519−1522.

(21) Subramanian, V.; Wolf, E. E.; Kamat, P. V. Catalysis with TiO2/Gold Nanocomposites. Effect of Metal Particle Size on the Fermi Level Equilibration. *J. Am. Chem. Soc.* **2004**, *126*, 4943−4950.

(22) Brown, M. D.; Suteewong, T.; Kumar, R. S. S.; D'Innocenzo, V.; Petrozza, A.; Lee, M. M.; Wiesner, U.; Snaith, H. J. Plasmonic Dye-Sensitized Solar Cells Using Core−Shell Metal−Insulator Nanoparticles. *Nano Lett.* **2011**, *11*, 438−445.

(23) Gangishetty, M. K.; Lee, K. E.; Scott, R. W. J.; Kelly, T. L. Plasmonic Enhancement of Dye Sensitized Solar Cells in the Red-to-near-Infrared Region using Triangular Core-Shell Ag@SiO2 Nanoparticles. *ACS Appl. Mater. Interfaces* **2013**, *5*, 11044−11051.

(24) Sheehan, S. W.; Noh, H.; Brudvig, G. W.; Cao, H.; Schmuttenmaer, C. A. Plasmonic Enhancement of Dye-Sensitized Solar Cells Using Core-Shell-Shell Nanostructures. *J. Phys. Chem. C* **2013**, *117*, 927−934.

(25) Jang, Y. H.; Jang, Y. J.; Kochuveedu, S. T.; Byun, M.; Lin, Z.; Kim, D. H. Plasmonic dye-sensitized solar cells incorporated with Au-TiO2nanostructures with tailored configurations. *Nanoscale* **2014**, *6*, 1823−1832.

(26) Dang, X.; Qi, J.; Klug, M. T.; Chen, P.-Y.; Yun, D. S.; Fang, N. X.; Hammond, P. T.; Belcher, A. M. Tunable Localized Surface Plasmon-Enabled Broadband Light-Harvesting Enhancement for High-Efficiency Panchromatic Dye-Sensitized Solar Cells. *Nano Lett.* **2013**, *13*, 637−642.

(27) Erwin, W. R.; Zarick, H. F.; Talbert, E. M.; Bardhan, R. Light Trapping in Mesoporous Solar Cells with Plasmonic Nanostructures. *Energy Environ. Sci.* **2016**, *9*, 1577−1601.

(28) Olalde-Velasco, P.; Jiménez-Mier, J.; Denlinger, J. D.; Hussain, Z.; Yang, W. L. Direct Probe of Mott-Hubbard to Charge-Transfer Insulator Transition and Electronic Structure Evolution in Transition-Metal Systems. *Phys. Rev. B: Condens. Matter Mater. Phys.* **2011**, *83*, 241102.

(29) Yang, W.; Devereaux, T. P. Anionic and Cationic Redox and Interfaces in Batteries: Advances from Soft X-ray Absorption Spectroscopy to Resonant Inelastic Scattering. *J. Power Sources* **2018**, *389*, 188−197.

(30) Kapilashrami, M.; Zhang, Y.; Liu, Y.-S.; Hagfeldt, A.; Guo, J. Probing the Optical Property and Electronic Structure of TiO2 Nanomaterials for Renewable Energy Applications. *Chem. Rev.* **2014**, *114*, 9662−9707.

(31) Villanueva-Cab, J.; Montaño-Priede, J. L.; Pal, U. Effects of Plasmonic Nanoparticle Incorporation on Electrodynamics and Photovoltaic Performance of Dye Sensitized Solar Cells. *J. Phys. Chem. C* **2016**, *120*, 10129−10136.

(32) Montaño-Priede, J. L.; Coelho, J. P.; Guerrero-Martínez, A.; Peña-Rodríguez, O.; Pal, U. Fabrication of Monodispersed Au@SiO2 Nanoparticles with Highly Stable Silica Layers by Ultrasound-Assisted Stöber Method. *J. Phys. Chem. C* **2017**, *121*, 9543−9551.

(33) Nakade, S.; Kanzaki, T.; Wada, Y.; Yanagida, S. Stepped Light-induced Transient Measurements of Photocurrent and Voltage in Dye-Sensitized Solar Cells: Application for Highly Viscous Electrolyte Systems. *Langmuir* **2005**, *21*, 10803−10807.

(34) Anta, J. A.; Idígoras, J.; Guillén, E.; Villanueva-Cab, J.; Mandujano-Ramírez, H. J.; Oskam, G.; Pellejà, L.; Palomares, E. A Continuity Equation for the Simulation of the Current-Voltage Curve and the Time-dependent Properties of Dye-Sensitized Solar Cells. *Phys. Chem. Chem. Phys.* **2012**, *14*, 10285−10299.

(35) Zhu, K.; Neale, N. R.; Halverson, A. F.; Kim, J. Y.; Frank, A. J. Effects of Annealing Temperature on the Charge-Collection and Light-Harvesting Properties of TiO2 Nanotube-Based Dye-Sensitized Solar Cells. *J. Phys. Chem. C* **2010**, *114*, 13433−13441.

(36) van de Lagemaat, J.; Kopidakis, N.; Neale, N. R.; Frank, A. J. Effect of Nonideal Statistics on Electron Diffusion in Sensitized Nanocrystalline TiO$_2$. *Phys. Rev. B: Condens. Matter Mater. Phys.* **2005**, *71*, 035304.

(37) Bisquert, J. Chemical Diffusion Coefficient of Electrons in Nanostructured Semiconductor Electrodes and Dye-Sensitized Solar Cells. *J. Phys. Chem. B* **2004**, *108*, 2323−2332.

(38) Qiao, R.; Li, Q.; Zhuo, Z.; Sallis, S.; Fuchs, O.; Blum, M.; Weinhardt, L.; Heske, C.; Pepper, J.; Jones, M.; Brown, A.; Spucces, A.; Chow, K.; Smith, B.; Glans, P.-A.; Chen, Y.; Yan, S.; Pan, F.; Piper, L. F. J.; Denlinger, J.; Guo, J.; Hussain, Z.; Chuang, Y.-D.; Yang, W. High-Efficiency in Situ Resonant Inelastic X-ray Scattering (iRIXS) Endstation at the Advanced Light Source. *Rev. Sci. Instrum.* **2017**, *88*, 033106.

(39) Jia, J. J.; Callcott, T. A.; Yurkas, J.; Ellis, A. W.; Himpsel, F. J.; Samant, M. G.; Stöhr, J.; Ederer, D. L.; Carlisle, J. A.; Hudson, E. A.; Terminello, L. J.; Shuh, D. K.; Perera, R. C. C. First Experimental Results from IBM/TENN/TULANE/LLNL/LBL Undulator Beamline at the Advanced Light Source. *Rev. Sci. Instrum.* **1995**, *66*, 1394−1397.

(40) Helmers, H.; Karcher, C.; Bett, A. W. Bandgap Determination Based on Electrical Quantum Efficiency. *Appl. Phys. Lett.* **2013**, *103*, 032108.

(41) Jang, Y. H.; Jang, Y. J.; Kim, S.; Quan, L. N.; Chung, K.; Kim, D. H. Plasmonic Solar Cells: From Rational Design to Mechanism Overview. *Chem. Rev.* **2016**, *116*, 14982−15034.

(42) Kopidakis, N.; Neale, N. R.; Frank, A. J. Effect of an Adsorbent on Recombination and Band-Edge Movement in Dye-Sensitized TiO2 Solar Cells: Evidence for Surface Passivation. *J. Phys. Chem. B* **2006**, *110*, 12485−12489.

(43) Wang, Q.; Butburee, T.; Wu, X.; Chen, H.; Liu, G.; Wang, L. Enhanced Performance of Dye-Sensitized Solar Cells by Doping Au Nanoparticles into Photoanodes: a Size Effect Study. *J. Mater. Chem. A* **2013**, *1*, 13524−13531.

(44) Landmann, M.; Rauls, E.; Schmidt, W. G. The Electronic Structure and Optical Response of Rutile, Anatase and Brookite TiO$_2$. *J. Phys.: Condens. Matter* **2012**, *24*, 195503.

(45) Olalde-Velasco, P.; Jiménez-Mier, J.; Denlinger, J.; Yang, W.-L. Atomic Multiplets at the L$_{2,3}$ edge of 3d Transition Metals and the Ligand K Edge in X-Ray Absorption Spectroscopy of Ionic Systems. *Phys. Rev. B: Condens. Matter Mater. Phys.* **2013**, *87*, 245136.

(46) Chen, X.; Glans, P.-A.; Qiu, X.; Dayal, S.; Jennings, W. D.; Smith, K. E.; Burda, C.; Guo, J. X-ray spectroscopic study of the electronic structure of visible-light responsive N-, C- and S-doped TiO2. *J. Electron Spectrosc. Relat. Phenom.* **2008**, *162*, 67−73.

(47) Listorti, A.; Creager, C.; Sommeling, P.; Kroon, J.; Palomares, E.; Fornelli, A.; Breen, B.; Barnes, P. R. F.; Durrant, J. R.; Law, C.; O'Regan, B. The Mechanism Behind the Beneficial Effect of Light Soaking on Injection Efficiency and Photocurrent in Dye Sensitized Solar Cells. *Energy Environ. Sci.* **2011**, *4*, 3494−3501.

(48) Villanueva-Cab, J.; Anta, J. A.; Oskam, G. The Effect of Recombination Under Short-Circuit Conditions on the Determination of Charge Transport Properties in Nanostructured Photoelectrodes. *Phys. Chem. Chem. Phys.* **2016**, *18*, 2303−2308.

(49) Grätzel, M. Photoelectrochemical Cells. *Nature* **2001**, *414*, 338−344.

(50) Wang, M.; Li, X.; Lin, H.; Pechy, P.; Zakeeruddin, S. M.; Grätzel, M. Passivation of nanocrystalline TiO2 junctions by surface adsorbed phosphinate amphiphiles enhances the photovoltaic performance of dye sensitized solar cells. *Dalton Trans.* **2009**, 10015−10020.

(51) Schwartzkopf, M.; Buffet, A.; Körstgens, V.; Metwalli, E.; Schlage, K.; Benecke, G.; Perlich, J.; Rawolle, M.; Rothkirch, A.; Heidmann, B.; Herzog, G.; Müller-Buschbaum, P.; Röhlsberger, R.; Gehrke, R.; Stribeck, N.; Roth, S. V. From Atoms to Layers: in situ Gold Cluster Growth Kinetics during Sputter Deposition. *Nanoscale* **2013**, *5*, 5053−5062.

(52) Schwartzkopf, M.; Santoro, G.; Brett, C. J.; Rothkirch, A.; Polonskyi, O.; Hinz, A.; Metwalli, E.; Yao, Y.; Strunskus, T.; Faupel, F.; Müller-Buschbaum, P.; Roth, S. V. Real-Time Monitoring of Morphology and Optical Properties during Sputter Deposition for Tailoring Metal-Polymer Interfaces. *ACS Appl. Mater. Interfaces* **2015**, *7*, 13547−13556.

(53) Hohn, N.; Schlosser, S. J.; Bießmann, L.; Grott, S.; Xia, S.; Wang, K.; Schwartzkopf, M.; Roth, S. V.; Müller-Buschbaum, P. Readily available Titania Nanostructuring Routines based on Mobility and Polarity controlled Phase Separation of an Amphiphilic Diblock Copolymer. *Nanoscale* **2018**, *10*, 5325−5334.